


PAPER

[View Article Online](#)
[View Journal](#)

Cite this: DOI: 10.1039/d0ta10033a

An ultra-long life aqueous full K-ion battery†

Yibo Li,‡ Wenjun Deng,‡ Zhuqing Zhou, Chang Li, Man Zhang, Xinran Yuan, Jun Hu, Haibiao Chen and Rui Li *Received 15th October 2020
Accepted 17th December 2020

DOI: 10.1039/d0ta10033a

rsc.li/materials-a

Aqueous full K-ion batteries (AFKIBs) featuring high safety, low cost, and environmental friendliness represent the future of advanced energy storage technologies. However, current AFKIB systems are still in need of suitable electrolytes and electrode materials, not to mention durability. Here, we report a “rocking-chair” type aqueous full K-ion system with $\text{KTi}_2(\text{PO}_4)_3/\text{C}$ crystalline nanoparticles as the anode material with near zero-strain, iron hexacyanoferrate as the cathode, and 21 m KCF_3SO_3 as a water-in-salt electrolyte. Benefitting from the fast reaction kinetics and high structural stability of $\text{KTi}_2(\text{PO}_4)_3/\text{C}$, the full battery achieves a high capacity retention of 96.7% over 30 000 cycles, excellent rate performance with full charge and discharge in 1 minute, and a high energy density of 47.3 Wh kg^{-1} . Demonstration of the performance of this AFKIB system expands the avenues of exploration for large-scale energy storage.

Introduction

In recent years, with the continuous development and utilization of renewable energy sources, the research on and applications of energy storage technologies have become increasingly extensive.^{1–4} Due to the unreliable and intermittent characteristics of wind and solar energies, it is challenging to integrate these renewable energies into the existing electric grid smoothly. Electrical energy storage technology employing secondary batteries is one of the most promising approaches to realize smart grid management.^{5,6} An ideal large-scale energy storage system requires low cost, long cycle life, high power, high safety and environmental friendliness.⁷ Lithium-ion batteries (LIBs) offer high energy densities and long cycle life, but still suffer from high cost, scarcity of lithium, and safety issues. For instance, organic electrolytes are flammable and toxic which could limit the application of LIBs in large-scale energy storage.⁵ Lead acid batteries are the least expensive, but their cycle life is short and they are not environmentally friendly. Sodium–sulphur and sodium–metal halide batteries operate at low current densities and require high temperatures to run, which is challenging for thermal management. Redox-flow batteries have low rate performance and low energy efficiencies.

Rechargeable aqueous alkali-ion batteries are promising candidates for large-scale energy storage owing to their inherent safety, high ionic conductivity, and low cost.^{8,9} Aqueous lithium-ion batteries (ALIBs) using lithium intercalation compounds

adopted from organic cells have been comprehensively studied, but they generally lack cycling stability.^{10,11} Aqueous sodium-ion batteries (ASIBs) with the abundance of the sodium element on earth can meet the low-cost requirements but they still suffer from insufficient cycle life.^{12–14} K-based aqueous batteries possess the advantages of using safe aqueous electrolytes, and the raw materials are more abundant and cheaper than lithium. Moreover, compared to Na^+ , K^+ is smaller in size when solvated due to its weaker Lewis acidity which enables rapid transport of K^+ ions and high ionic conductivity.¹⁵ However, suitable electrolytes and anodes for aqueous full K-ion batteries (AFKIBs) are still hard to find. A major challenge is that the (de)intercalation of large K^+ ions always induces a substantial volume change in the electrode material and causes irreversible structural degradation. Besides, water decomposition during K^+ (de)insertion can cause undesirable capacity loss.^{16,17} An AFKIB was first reported by Hu's group¹⁸ using a K-MnHCF cathode, PTCDI anode and 22 m KCF_3SO_3 aqueous electrolyte, but the cycle life of the full battery is limited by the anode (73% capacity retention after 2000 cycles at 4C). Another AFKIB (K-FeHCF/30 m KFSI/ β -PTCDA) using an organic anode has been proposed, but the lifespan was only 1000 cycles with 89% capacity retention at 12.5C.¹⁹ Among the anode candidates, NASICON-type $\text{KTi}_2(\text{PO}_4)_3$ (KTP) could be a promising electrode material for aqueous K-ion batteries, since the robust 3D framework structure and appropriate redox potentials can sustain a continuous K^+ insertion/extraction process. Nanocubic $\text{KTi}_2(\text{PO}_4)_3/\text{C}$ was first reported for K^+ storage in nonaqueous K-ion batteries, whereas the low diffusion coefficient of K^+ ($2.37 \times 10^{-13} \text{ cm}^2 \text{ s}^{-1}$) led to serious polarization.²⁰ Then Ji *et al.*¹⁷ reported the K^+ storage performance of KTP in a low-cost superconcentrated aqueous electrolyte (30 m potassium acetate), a configuration reported by our group earlier,²¹ but the capacity was only 58 mA h g^{-1} with a poor rate capability. Overall, AFKIB research

School of Advanced Materials, Peking University Shenzhen Graduate School, Shenzhen, 518055, China. E-mail: liruisz@pku.edu.cn

† Electronic supplementary information (ESI) available. See DOI: 10.1039/d0ta10033a

‡ These authors contributed equally to this work.

is still in its infancy, and lags far behind that on ALIBs and ASIBs. The durability of the aqueous alkali-ion rechargeable batteries is by far the most critical challenge. Therefore, the development of high performance and durable AFKIBs to meet the demand of large-scale energy storage is very meaningful.

In this work, we introduce a “rocking-chair” type AFKIB system using a low-cost and environment-friendly $\text{KTi}_2(\text{PO}_4)_3/\text{C}$ (designated as KTP/C) anode, $\text{K}_2\text{FeFe}(\text{CN})_6$ (designated as K-FeHCF) cathode, and water-in-salt electrolyte of 21 m KCF_3SO_3 , and realize an ultra-long life AFKIB for the first time. The synthesized $\text{KTi}_2(\text{PO}_4)_3/\text{C}$ (KTP/C) crystalline nanoparticles are conducive to the fast transportation of K^+ , and the diffusion coefficient of K^+ reaches up to $3.25 \times 10^{-10} \text{ cm}^2 \text{ s}^{-1}$. More importantly, the open-framework structure maintains almost zero-strain during the K^+ insertion/extraction process with a cell volume change of 0.5%, demonstrating a remarkable stability. Based on this, the fabricated AFKIB exhibits an outstanding rate capability and an unprecedented cycling stability with a capacity retention of 100% over 3000 cycles, even at a high rate of 5 A g^{-1} (charge and discharge in 1 minute). The lifespan over 30 000 cycles with an energy density of 24 W h kg^{-1} represents a significant step forward in the exploration of AFKIBs as a promising low-cost alternative for large-scale energy storage.

Results and discussion

The low electronic conductivity of typical NASICON-type materials will restrain the kinetic processes and lead to a low capacity, and thus we prepared carbon-coated $\text{KTi}_2(\text{PO}_4)_3$ composites *via* a hydrothermal method followed by annealing.²² The carbon content of the as-prepared sample is 9.7% as

determined from TGA analysis (Fig. S1†). The X-ray diffraction (XRD) patterns of the KTP precursor and KTP/C in Fig. 1a show that all diffraction peaks agree well with a reported rhombohedral structure of $\text{KTi}_2(\text{PO}_4)_3$ (PDF#79-1880), indicating high purity of the products. Fig. 1b shows the KTP structural framework composed of TiO_6 octahedra and PO_4 tetrahedra with potassium ions fully occupying the interstitial sites, revealing that the 3D framework provides large interstitial spaces to transport potassium ions rapidly. The morphology and structure of KTP/C were characterized by scanning electron microscopy (SEM) and transmission electron microscopy (TEM). The KTP/C material is constructed with a large number of crystalline nanoparticles with diameters of 10–30 nm (Fig. S2† and 1c, d), which is beneficial for the fast transport of potassium ions. The high-resolution transmission electron microscopy (HRTEM) images are shown in Fig. 2e and f. The spacings in the lattice fringes were calculated to be about 0.370 nm and 0.303 nm matching well with the interplanar spacing of the (113) and (024) planes of $\text{KTi}_2(\text{PO}_4)_3$, respectively. In addition, a compact amorphous layer with a thickness of about 3.3 nm on the surface of nanoparticles can be clearly observed, corresponding to the carbon coating, which is expected to provide a high electronic conductivity for the composites. The elemental composition and distribution were also investigated by energy dispersive spectrometry (EDS) and X-ray photoelectron spectroscopy (XPS): K, Ti, P, O and C elements are distributed homogeneously in KTP/C (Fig. S3†).

The electrochemical behaviours of KTP/C electrodes were evaluated in three-electrode cells with activated carbon as the counter electrode and a saturated calomel electrode (SCE) as the reference electrode. There is only one pair of redox peaks around -0.90 V vs. SCE observed in the cyclic voltammograms (CVs) as shown in Fig. 2a, which can be ascribed to the conversion of the $\text{Ti}^{4+}/\text{Ti}^{3+}$ redox couple. A water-in-salt

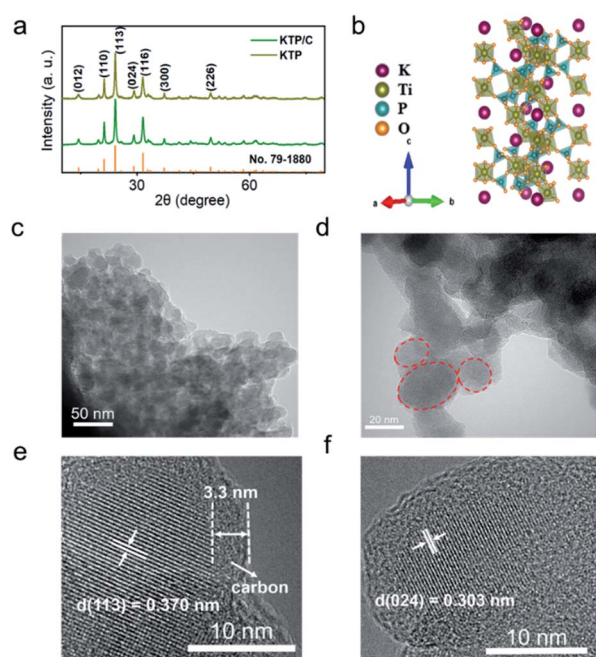


Fig. 1 (a) The XRD patterns of KTP and KTP/C. (b) The crystal structure of KTP. (c and d) The TEM images of KTP/C. (e and f) The HRTEM images of KTP/C.

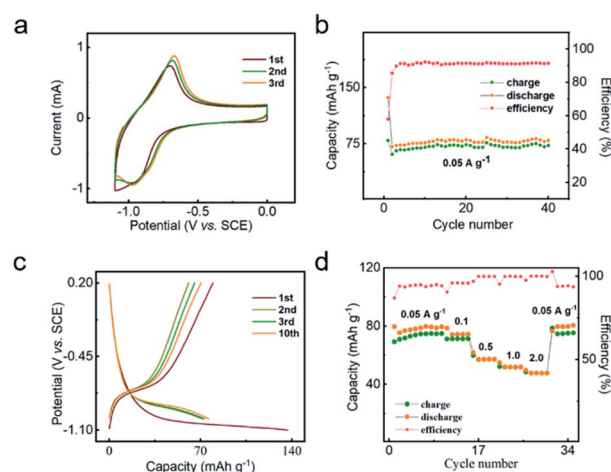


Fig. 2 (a) The CV curves of the first three cycles for KTP/C at a scan rate of 1 mV s^{-1} between -1.1 and 0 V vs. SCE . (b) The galvanostatic charge/discharge cycle of the KTP/C anode at 0.05 A g^{-1} . (c) The 1st, 2nd, 3rd and 10th charge/discharge curves of the KTP/C anode at 0.05 A g^{-1} . (d) The rate capability of the KTP/C anode at various current densities.

electrolyte 21 m KCF_3SO_3 was chosen to prevent hydrogen evolution in consideration of the low redox potential of KTP. Fig. 2b shows the cycling performance of KTP/C at a low current density of 0.05 A g^{-1} , and the first discharge and charge capacities were 137 mA h g^{-1} and 79.5 mA h g^{-1} , respectively. The irreversible discharge capacity in the first cycle should be attributed to the formation of a solid-electrolyte interface (SEI) on the surface of the anode material, and this phenomenon has also been observed in other fluorine-containing “water-in-salt” electrolytes.^{23–25} The reversible capacity stabilized at about 78 mA h g^{-1} and showed no decay after 40 cycles, indicating that the KTP/C electrode is highly stable and reversible. Note that the coulombic efficiency depends on the charge–discharge rate for the three-electrode system,^{18,26} and the removal of dissolved oxygen from the electrolyte is beneficial for coulombic efficiency. The long-term cycle performance is also provided in Fig. S4.† The galvanostatic charge/discharge (GCD) curves are shown in Fig. 2c. The potential plateaus in the curves are well consistent with the CV results, and the discharge capacity remains stable after the first discharge. Fig. 2d shows the reversible capacities of the KTP/C anode at various current densities. The discharge capacities are 76.3, 71.8, 57.3, 51.7, and 47.5 mA h g^{-1} at current densities of 0.05, 0.1, 0.5, 1.0, and 2.0 A g^{-1} , respectively. The corresponding GCD curves are shown in Fig. S5.† and a low polarization phenomenon was observed with the increasing rate. The high rate capability is attributed to the small nanoparticle size and the large ion

channels within the KTP/C nanoparticles, whereas the pure KTP anode exhibits poor performance of rate capability and cycling stability (Fig. S6†). To investigate the electrochemical kinetic behavior, the K^+ diffusion coefficient was investigated through the electrochemical impedance spectroscopy (EIS) method and the galvanostatic intermittent titration technique (GITT) (Fig. S7†). The diffusion coefficients of K^+ values are in the magnitude range of 10^{-10} to 10^{-11} for the KTP/C, which is much higher than those of other anode materials reported so far and significantly reflects the fast K-intercalation kinetics.^{20,27}

To build a workable AFKIB, the Prussian Blue analogue $\text{K}_{1.93}\text{Fe}[\text{Fe}(\text{CN})_6]_{0.97} \cdot 1.82\text{H}_2\text{O}$ (K-FeHCF) was adopted as the cathode. K-rich and low vacancy K-FeHCF nanocubes were synthesized by a size-regulation hydrothermal method which was described in detail in our previous work.²⁸ Fig. S8† displays the structure and morphology of the as-synthesized K-FeHCF. The electrochemical properties of the K-FeHCF electrode examined with three-electrode cells in the 21 m KCF_3SO_3 electrolyte are shown in Fig. S9.† The K-FeHCF electrode delivered a high reversible capacity of $131.1 \text{ mA h g}^{-1}$ at 0.2 A g^{-1} and a superior capacity retention of 56.5% even at a high current density of 5.0 A g^{-1} . There are two plateaus observed in the charge and discharge curves corresponding to the redox reactions of the high-spin-state nitrogen-coordinated couple ($\text{Fe}^{3+}/\text{Fe}^{2+}\text{-N}$) and low-spin-state carbon-coordinated couple ($\text{Fe}^{3+}/\text{Fe}^{2+}\text{-C}$), respectively.^{29,30} The long-term cycling performance of the K-FeHCF cathode was also evaluated at a current density of

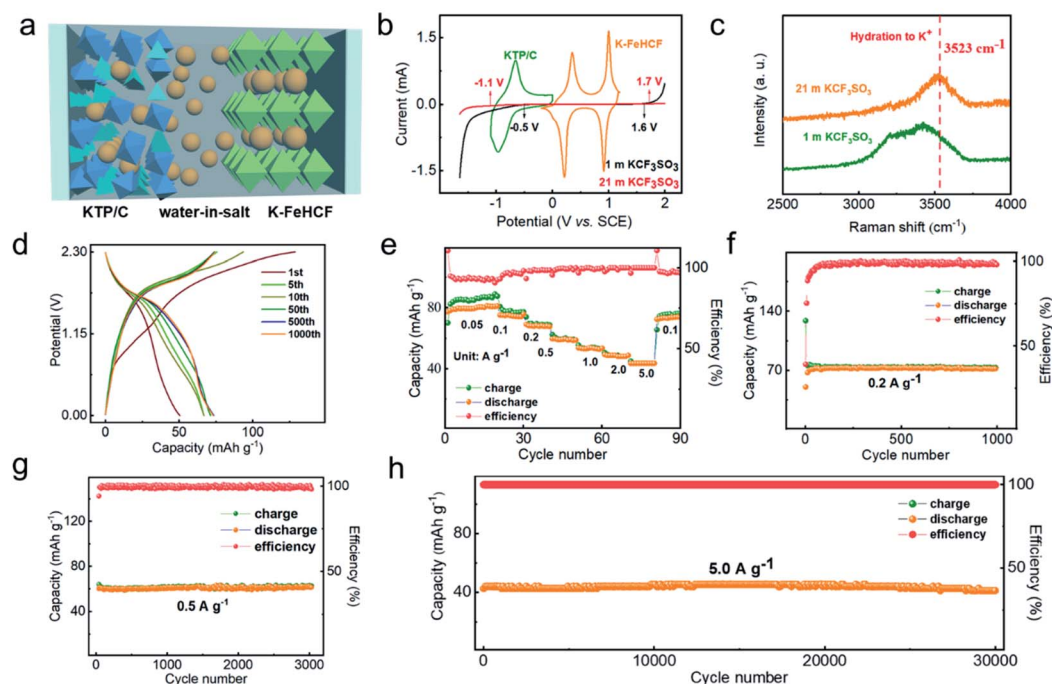


Fig. 3 (a) Schematic of the AFKIB. (b) The electrochemical stability windows of the 1 m and 21 m KCF_3SO_3 electrolytes were measured by linear sweep voltammetry between -1.6 and 2.0 V vs. SCE on a Pt electrode at a scan rate of 1 mV s^{-1} , which are overlaid with the CV curves of KTP/C and K-FeHCF electrodes in 21 m KCF_3SO_3 at the same scanning rate. (c) The Raman spectra of 1 m and 21 m KCF_3SO_3 electrolytes in the range of $2500\text{--}4000 \text{ cm}^{-1}$. (d) The charge/discharge curves of the K-FeHCF//21 m KCF_3SO_3 //KTP/C full cell at a current density of 0.2 A g^{-1} . (e) The rate capability of the full cell at various current densities. The long-term cycling performance of the full cells at different current densities of (f) 0.2, (g) 0.5 and (h) 5.0 A g^{-1} .

2.0 A g⁻¹. The capacity only decreased from 99.4 to 64.5 mA h g⁻¹ even after 800 cycles, and the high stability is ascribed to the high crystallinity and nanosized structure of the material.

A “rocking-chair” type AFKIB (Fig. 3a) was assembled with the above cathode and anode in a 21 m KCF₃SO₃ electrolyte which has a high conductivity of 61.2 mS cm⁻¹ and a low viscosity of 8.3 mPa s. The mass loading of the anode and cathode active material is about 6.5 mg cm⁻². The optimized mass ratio of the positive (K-FeHCF) and negative (KTP/C) electrode is about 1 : 1 (P : N = 1 : 1) to retain the positive (K-FeHCF) excess, which can maximize the cycle life of the full battery despite sacrificing some energy density. Fig. 3b shows the CV curves of the cathode and anode in half cells in 21 m KCF₃SO₃, as well as the linear sweep voltammetry (LSV) profiles in 1 m and 21 m KCF₃SO₃ performed on Pt electrodes. The superconcentrated electrolyte of 21 m KCF₃SO₃ provides an expanded electrochemical stability window (ESW) of 2.8 V (−1.1 to 1.7 V vs. SCE), while the ESW was only 2.1 V for 1 m KCF₃SO₃. The expanded ESW is attributed to the water molecules strongly coordinated to K⁺ ions and almost entirely confined in K⁺ ion solvation sheaths.²⁵ As shown in Fig. 3c, the Raman spectrum of 21 m KCF₃SO₃ shows a sharp peak around 3523 cm⁻¹, which represents the O–H stretching vibration of water indicating a strong K⁺ ion solvation. By contrast, there is a broad band in the 3000–3600 cm⁻¹ range caused by the O–H stretching vibration corresponding to free water molecules with different hydrogen-bonding environments in water clusters.³¹ The CV curve of the KTP/C anode shows one redox couple at −0.91/−0.7 V (vs. SCE), and the low redox potential did not exceed the cathodic limit and should be enveloped in the wide ESW, allowing reversible K storage. On the cathode side, there are two pairs of redox peaks at 0.21/0.35 V and 0.91/1.0 V (vs. SCE), respectively, representing the two-electron redox reactions of K-FeHCF, which are far from the oxygen evolution potential (1.7 V). Consequently, the voltage window for K⁺ insertion/extraction can rest comfortably within the cathodic and anodic limits of the superconcentrated electrolyte.

Fig. 3d shows the GCD curves of this AFKIB at a current density of 0.2 A g⁻¹ in different cycles during a cycling test. The full cell delivered a high reversible capacity of 73 mA h g⁻¹ (based on KTP/C mass) with approximately 100% utilization of the capacity of the anode in the half cell, and the average discharge voltage reached 1.5 V. The rate capability of the AFKIB was evaluated and the data are shown in Fig. 3e. A high discharge capacity of 81 mA h g⁻¹ was achieved at 0.05 A g⁻¹, and the specific capacity decreased modestly as the rate increased. The reversible capacity still reached 43.6 mA h g⁻¹ at a high rate of 5.0 A g⁻¹, and as the current density returned to 0.1 A g⁻¹, the capacity was restored to 74.1 mA h g⁻¹ again. Fig. S10† shows the corresponding voltage profiles, and a slight decrease in the average discharge voltage from 1.5 V to 1.3 V can be observed when the current density increased sharply from 0.05 A g⁻¹ to 5.0 A g⁻¹, suggesting fast K-insertion kinetics with low polarization. The AFKIB exhibited an energy density of 47.3 W h kg⁻¹ at a power density of 30.4 W kg⁻¹ (based on the total mass of the cathode and anode active materials) and still

delivered 24 W h kg⁻¹@2.9 kW kg⁻¹ (Fig. S11†). Fig. 3f–h display the long-term cycling stability of the AFKIB at different current densities. The discharge capacity increased gradually at the beginning and then stabilized at 73 mA h g⁻¹ after about 40 cycles with a coulombic efficiency of ~99% at 0.2 A g⁻¹. After 40 cycles of activation, the battery delivered a reversible capacity of 61 mA h g⁻¹ with a high coulombic efficiency of ~100% at 0.5 A g⁻¹, and there was no capacity decay after 3000 cycles. Even at an ultrahigh rate of 5.0 A g⁻¹ (a full charge/discharge process took 1 minute), this AFKIB exhibited an initial capacity of 42.6 mA h g⁻¹ with an ultra-long lifespan of 30 000 cycles, with a 96.7% final capacity retention. To further understand the diffusion-controlled and capacitive-controlled charge of the batteries, we have performed CV measurements at multiple scan rates from 0.5 to 5 mV s⁻¹. The following equation is used to study the behavior:³²

$$i(V) = k_1 v^{1/2} + k_2 v$$

where $i(V)$ represents the current measured at a certain potential V , v represents the scan rates, and $k_1 v$ and $k_2 v^{1/2}$ represent the contributions of capacitive and diffusion-controlled behaviors. By rewriting the above equation and simplifying it, we get the follow equation:

$$i(V)/v^{1/2} = k_1 + k_2 v^{1/2}$$

The values of k_2 and capacitance current can be obtained by plotting the plots of $i(V)/v^{1/2}$ and $v^{1/2}$. From the above calculations, the contribution ratios of the capacitor currents at the scan rates of 0.5, 1, 2, 3, 4 and 5 mV s⁻¹ are 64%, 69%, 76%, 79%, 82% and 84%, respectively (Fig. 4). With the increase of the scan rate, the capacitive contributions dominate. The high capacitance contribution means that the KTP@C electrode material can withstand the impact of higher density currents, thus realizing an ultra-long life span. We compared the electrochemical performance of this AFKIB with that of other reported AFKIBs^{18,19} and AFSIBs^{14,26,33–38} in Table 1. Such a AFKIB exhibits the best cycling stability among the reported aqueous alkali-ion rechargeable batteries, indicating that a new AFKIB for safe, low-cost, and long-lasting large-scale energy storage can be potentially materialized.

To understand the origin of the high performance of the AFKIB, the K⁺ storage mechanism of the optimized anode was

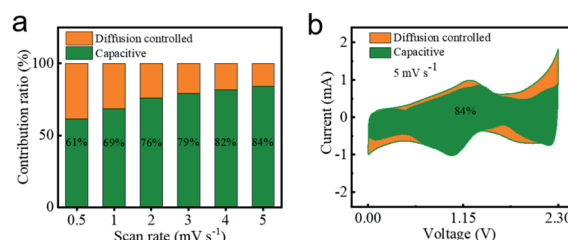


Fig. 4 (a) Capacitive contribution ratios at multiple scan rates. (b) Capacity separation curves at 5 mV s⁻¹.

Table 1 Electrochemical performance comparison of K-FeHCF//KTP/C with recently reported AFKIBs and aqueous full sodium-ion batteries (AFSIBs)

System	Electrolyte	Energy density (W h kg ⁻¹)	Average voltage (V)	Cycle performance (retention, cycles, rate)	Ref.
K-FeHCF//KTP/C (AFKIB)	21 m KCF₃SO₃	47.3	1.5	96.7%, 30 000 cycles, 5 A g⁻¹	This work
KFHCF//β-PTCDA (AFKIB)	30 m KFSI	41	0.9	89%, 1000 cycles, 12.5C	18
KFeMnHCF//PTCDI (AFKIB)	22 m KCF ₃ SO ₃	80	1.3	73%, 2000 cycles, 4C	19
Na ₂ Mn[Fe(CN) ₆]/[KMn[Cr(CN) ₆]] (AFSIB)	17 m NaClO ₄	58	1.7	87%, 100 cycles, 30C	33
CoCuHCF//SNDI (AFSIB)	1 M Na ₂ SO ₄	30	1.1	88%, 100 cycles, 20C	34
Na ₃ MnTi(PO ₄) ₃ /Na ₃ MnTi(PO ₄) ₃ (AFSIB)	1 M Na ₂ SO ₄	40	1.4	98%, 100 cycles, 1C	35
Na _{0.66} Mn _{0.66} Ti _{0.44} O ₂ //NTP (AFSIB)	9.26 m NaOTf	31	1.0	92.7%, 1200 cycles, 1C	26
NaMnO ₂ //NTP (AFSIB)	2 M NaAc	30	0.81	75%, 500 cycles, 10C	36
NVP//NTP (AFSIB)	1 M Na ₂ SO ₄	29	1.2	50%, 50 cycles, 10 A g ⁻¹	14
NVP//NTP (AFSIB)	22 m TEAOTf + 9 m NaOTf	—	1.25	78%, 100 cycles, 1C	37
NVP//NTP (AFSIB)	Na-H ₂ O-urea-DMF	61	1.23	86%, 100 cycles, 10C	38

further investigated through X-ray photoelectron spectroscopy (XPS), *ex situ* XRD, and *ex situ* TEM techniques as shown in Fig. 5. The significant signals of the Ti 2p_{3/2}-Ti 2p_{1/2} doublet located at 459.3 eV and 465.2 eV could be assigned to Ti⁴⁺ in the pristine KTP/C (Fig. 5a).³⁹ When the cell was charged to 2.3 V (Fig. 5b), the fitted XPS spectrum of Ti 2p from the disassembled anode exhibits two pairs of peaks at 459.3/465.1 eV and 458.3/463.9 eV assigned to Ti⁴⁺ and Ti³⁺, respectively. The ratio of Ti⁴⁺/Ti³⁺ should be 2/5 calculated from the peak areas, amounting to 5/7 utilization of the theoretical capacity (128 mA h g⁻¹) of the KTP/C, which is close to the test result of 81 mA h g⁻¹. After full discharge (Fig. 5c), all of the Ti³⁺ was oxidized to Ti⁴⁺ again, indicating a high reversibility of the anode.

The (de)insertion mechanism in KTP/C was investigated through *ex situ* XRD as shown in Fig. 5d. The patterns were collected at different charge/discharge states, and the observed peak evolution demonstrates a typical solid-solution reaction mechanism upon K⁺ (de)intercalation. The peak positions barely changed, especially for the (113) and (024) planes, implying that there was no crystal transformation or significant change of lattice parameters. The corresponding cell volume expansion of the anode host during discharging (K⁺ insertion) is also given in Fig. 5e, and the lattice strain reaches a maximum of 0.5% when 1.27 K⁺ ions per formula unit were inserted. Such a near zero-strain feature is directly responsible for the demonstrated fast kinetics and excellent structural stability. Furthermore, *ex situ* TEM was performed as shown in Fig. 5f-k. The KTP/C particles remained intact without pulverization or fragmentation after being fully charged (Fig. 5f) and discharged (Fig. 5i). Furthermore, the interplanar spacing of the (113) and (024) planes are clearly visible after being charged to 2.3 V (Fig. 5g and h) and discharged to 0 V (Fig. 5j and k). There were only 0.54% and 0.33% changes for the (113) and (024) planes, respectively, which further proves the extremely low lattice strain occurring during the K⁺ insertion/extraction of the anode. Meanwhile, the structural and morphological changes of the corresponding cathode (K-FeHCF) were also investigated (Fig. S12†). The K-FeHCF in the full-cell showed a negligible change during charge/discharge.

Experimental

Synthesis of K₂FeFe(CN)₆ (K-FeHCF)

Typically, 4 mmol potassium ferrocyanide (K₄Fe(CN)₆) and 1 g ascorbic acid (C₆H₈O₆) were added into 120 mL of a 1 mol L⁻¹ hydrochloric acid (HCl) aqueous solution. Dissolved oxygen in the water was removed by bubbling N₂ for 30 minutes, and then the obtained solution was heated at 70 °C with stirring under N₂ protection. After 4 hours, the product was collected by filtration and washed three times with deionized water and ethanol (C₂H₅OH). Finally, the samples were dried under vacuum at 110 °C for 12 hours.

Synthesis of the KTi₂(PO₄)₃/carbon (KTP/C) nanocomposite

In a typical procedure, KTP/C was synthesized by a solvothermal method and subsequent glucose-pyrolysis treatment. Firstly, 5 mmol potassium acetate (CH₃COOK) was dissolved in 40 mL ethanol (C₂H₅OH) with stirring for 30 minutes. Then, 4 mmol tetrabutyl titanate (C₁₆H₃₆O₄Ti) and 5 mL phosphoric acid (H₃PO₄) were added to the above solution in turn with continuous stirring. The milky white suspension was transferred to a 100 mL Teflon-lined stainless-steel autoclave and heated at 180 °C for 24 hours. After centrifugation and washing three times using deionized water, the product was dried at 80 °C for 12 hours followed by annealing in argon at 500 °C for 4 hours with a heating rate of 5 °C min⁻¹. The precursor and anhydrous glucose were mixed by grinding for 30 minutes. Finally, the mixture was annealed in argon at 750 °C for 5 hours with a heating rate of 5 °C min⁻¹ to obtain the desired product KTP/C.

Materials characterization

The crystal structures of both the K-FeHCF and KTP/C materials were measured using an X-ray diffractometer (XRD, Bruker D8 Advance diffractometer) with Cu Kα radiation (λ = 1.5416 Å). The chemical composition of K-FeHCF was examined by inductively coupled plasma-atomic emission spectroscopy (ICP-AES, HORIBA Jobin Yvon JY2000-2) and the H, C and N elements were obtained by element analysis (Vario EL cube). The crystal water content of the K-FeHCF and the carbon content of the

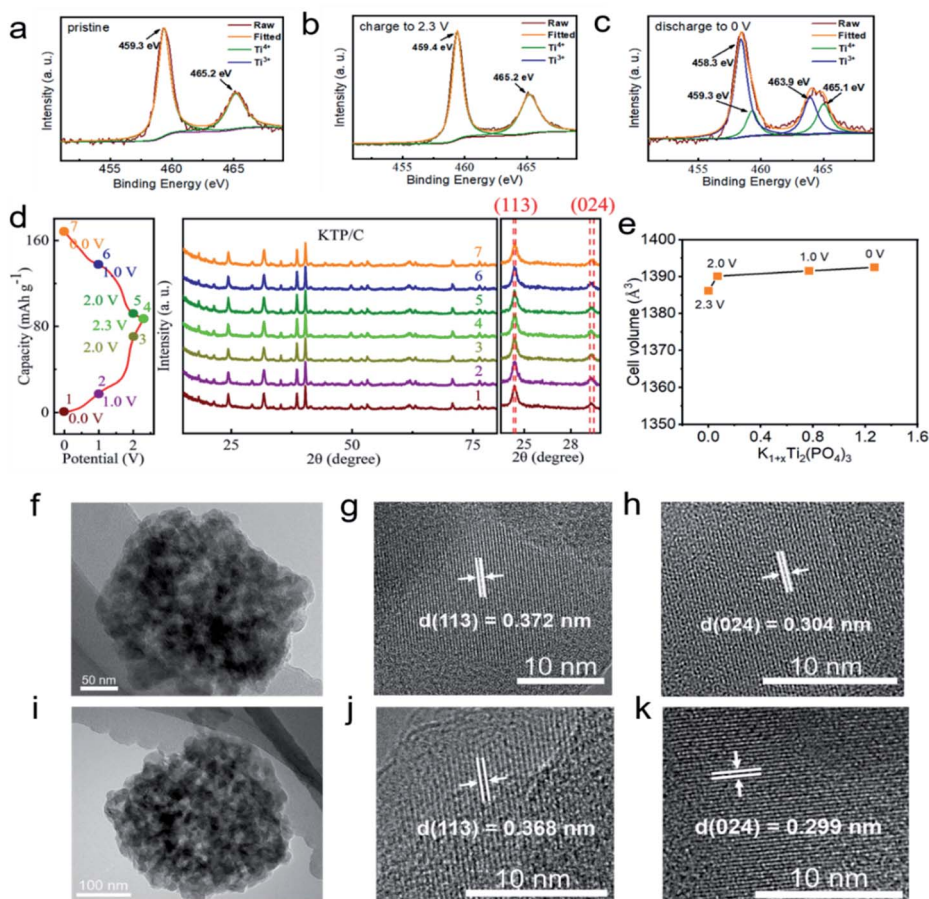


Fig. 5 The *ex situ* XPS spectra of the Ti 2p of KTP/C in the full AKIB, (a) pristine sample, (b) charged to 2.3 V and (c) discharged to 0 V after 10 cycles. (d) The *ex situ* XRD patterns of KTP/C in the full AKIBs at different states; the cells were first cycled for 10 cycles then charged/discharged to the desired states at 0.05 A g⁻¹. The marked dots from 1 to 7 in the GCD curves (left) represent the states measured by *ex situ* XRD (right). (e) The corresponding cell volume expansion of the anode host during discharging (K⁺ insertion). The *ex situ* TEM images of KTP/C in the full AKIBs after 10 cycles ending with a fully charged state (f–h) and a fully discharged state (i–k).

KTP/C were measured by thermogravimetric analysis (TGA, Mettler-Toledo TGA/DSC-1 system). The change in the elemental valence state between charge and discharge states was examined using an X-ray Photoelectron Spectrometer (Thermo Fisher ESCALAB 250Xi). The microstructure, morphology, and elemental distribution of both the cathode and anode materials were obtained using a transmission electron microscope (TEM, FEI Tecnai G2F20 s-Twin) and scanning electron microscope (SEM, ZEISS Supra 55) equipped with an Oxford Aztec energy dispersive spectrometer (EDS). The Raman spectra of the electrolytes were collected by using a Lab Ram HR Evolution Series High Resolution Raman Spectrometer (HORIBA Jobin Yvon SAS, France). The viscosity and ionic conductivities of the electrolytes were obtained by using a rotational rheometer Haake MARS III (Thermo Fisher Scientific, Germany) and an electrical conductivity meter DDS-307 (INESA Scientific Instrument Co., Ltd.), respectively.

Preparation of the electrodes and electrochemical tests

All electrodes were fabricated at room temperature and standard atmospheric pressure. Both K-FeHCF and KTP/C

electrodes were prepared by mixing the active material, Ketjen Black, and polytetrafluoroethylene (PTFE) in a weight ratio of 7 : 2 : 1 with isopropyl alcohol as a diluent and then pressed onto titanium mesh. The electrochemical properties of both electrodes in the 21 m KCF₃SO₃ electrolyte were tested at room temperature using a three-electrode system, in which the working electrode contained the active material, the counter electrode was prepared from a commercial activated carbon powder (YEC-8A), and the reference electrode was a saturated calomel electrode (SCE). For the full K-FeHCF//KTP/C cell, the 21 m KCF₃SO₃ electrolyte was used with the electrodes to be assembled into a CR2032 cell, and all the above tests were carried out using a NEWARE battery test system. Cyclic voltammetry (CV, 1 mV s⁻¹) and electrochemical impedance spectroscopy (EIS, 0.01 Hz to 100 kHz) tests were carried out using a CHI660D electrochemical workstation (Chenhua Instrument Company, Shanghai, China) using a commercial activated carbon electrode as the counter electrode, a saturated calomel electrode (SCE) as the reference electrode, and a K-FeHCF or KTP/C electrode as the working electrode, respectively.

Calculation of K⁺ ion diffusivity

The K⁺ diffusion coefficient of the KTP/C electrode was calculated based on the results of electrochemical impedance spectroscopy (EIS) and the galvanostatic intermittent titration technique (GITT) recorded in the three-electrode system. The EIS curve of KTP/C is shown in Fig. S7a.† For EIS, ion-diffusion coefficients of the electrode material could be calculated using the following formula:

$$D^{\text{EIS}} = \frac{R^2 T^2}{2n^4 \sigma^2 A^2 C^2 F^4}$$

where R is the gas constant (8.314 J K⁻¹ mol⁻¹), T is room temperature (298.15 K), n is the number of the electrons transferred in the electronic reaction, A is the surface area of the electrode (3.85×10^{-5} m²), C is the concentration of K⁺ in the KTP/C electrode, F is the Faraday constant (96 485 C mol⁻¹) and σ is the slope of the line $Z' - \omega^{-1/2}$ (as shown in the inset of Fig. S4b,† the σ value is 0.96). Hence, the calculated D_{K^+} of KTP/C is 3.25×10^{-10} cm² s⁻¹.

And for the GITT, the diffusion coefficient computational formula is as follows:

$$D^{\text{GITT}} = \frac{4}{\pi \tau} \left(\frac{m_{\text{B}} V_{\text{M}}}{M_{\text{B}} S} \right) \left(\frac{\Delta E_{\text{s}}}{\Delta E_{\text{r}}} \right)^2 (\tau \Delta L^2 / D)$$

where τ is the time for a corresponding galvanostatic current; m_{B} , M_{B} , and V_{M} are the mass, molecular weight, and molar volume of KTP, respectively; S is the electrode–electrolyte interface area (taken as the geometric area of the electrode); ΔE_{s} and ΔE_{r} are the quasi-equilibrium voltage and the change of the cell voltage E during the current pulse, respectively; L is the thickness of the electrode.

Conclusions

In summary, we have developed an AFKIB using KTi₂(PO₄)₃/C crystalline nanoparticles as the anode and the Prussian Blue analogue K_{1.93}Fe[Fe(CN)₆]_{0.97} · 1.82H₂O as the cathode in a 21 m KCF₃SO₃ aqueous electrolyte. This battery system exhibited a high energy density of 47.3 W h kg⁻¹, high-rate capability and unprecedented long lifespan over 30 000 cycles with negligible capacity loss. The outstanding performance is attributed to the as-fabricated nano-sized KTP/C, which supports fast reaction kinetics and maintains a near zero-strain during K⁺ storage. Such a safe, environmentally friendly, low-cost and extremely durable AFKIB is particularly attractive for large-scale energy storage.

Conflicts of interest

The authors declare no conflict of interest.

Acknowledgements

This work was supported by the Shenzhen Science and Technology Innovation Commission (JCYJ20180504165506495 and JCYJ20170818085823773).

Notes and references

- 1 D. P. Dubal, O. Ayyad, V. Ruiz and P. Gómez-Romero, *Chem. Soc. Rev.*, 2015, **44**, 1777–1790.
- 2 K. C. Divya and J. Østergaard, *Electr. Power Syst. Res.*, 2009, **79**, 511–520.
- 3 H. Pan, Y.-S. Hu and L. Chen, *Energy Environ. Sci.*, 2013, **6**, 2338–2360.
- 4 T. M. I. Mahlia, T. J. Saktisahdan, A. Jannifar, M. H. Hasan and H. S. C. Matseelar, *Renewable Sustainable Energy Rev.*, 2014, **33**, 532–545.
- 5 Z. Yang, J. Zhang, M. C. W. Kintner-Meyer, X. Lu, D. Choi, J. P. Lemmon and J. Liu, *Chem. Rev.*, 2011, **111**, 3577–3613.
- 6 B. Dunn, H. Kamath and J.-M. Tarascon, *Science*, 2011, **334**, 928–935.
- 7 S. Chu and A. Majumdar, *Nature*, 2012, **488**, 294–303.
- 8 C. D. Wessells, S. V. Peddada, R. A. Huggins and Y. Cui, *Nano Lett.*, 2011, **11**, 5421–5425.
- 9 B. Scrosati, J. Hassoun and Y.-K. Sun, *Energy Environ. Sci.*, 2011, **4**, 3287–3295.
- 10 H. Kim, J. Hong, K.-Y. Park, H. Kim, S.-W. Kim and K. Kang, *Chem. Rev.*, 2014, **114**, 11788–11827.
- 11 J.-Y. Luo, W.-J. Cui, P. He and Y.-Y. Xia, *Nat. Chem.*, 2010, **2**, 760–765.
- 12 Z. Li, D. Young, K. Xiang, W. C. Carter and Y.-M. Chiang, *Adv. Energy Mater.*, 2013, **3**, 290–294.
- 13 X. Wu, Y. Cao, X. Ai, J. Qian and H. Yang, *Electrochem. Commun.*, 2013, **31**, 145–148.
- 14 Q. Zhang, C. Liao, T. Zhai and H. Li, *Electrochim. Acta*, 2016, **196**, 470–478.
- 15 K. Kubota, M. Dahbi, T. Hosaka, S. Kumakura and S. Komaba, *Chem. Rec.*, 2018, **18**, 459–479.
- 16 H. Kim, J. C. Kim, M. Bianchini, D.-H. Seo, J. Rodriguez-Garcia and G. Ceder, *Adv. Energy Mater.*, 2018, **8**, 1702384.
- 17 D. P. Leonard, Z. Wei, G. Chen, F. Du and X. Ji, *ACS Energy Lett.*, 2018, **3**, 373–374.
- 18 L. Jiang, Y. Lu, C. Zhao, L. Liu, J. Zhang, Q. Zhang, X. Shen, J. Zhao, X. Yu, H. Li, X. Huang, L. Chen and Y.-S. Hu, *Nat. Energy*, 2019, **4**, 495–503.
- 19 H. Chen, Z. Zhang, Z. Wei, G. Chen, X. Yang, C. Wang and F. Du, *Sustainable Energy Fuels*, 2020, **4**, 128–131.
- 20 J. Han, Y. Niu, S.-j. Bao, Y.-N. Yu, S.-Y. Lu and M. Xu, *Chem. Commun.*, 2016, **52**, 11661–11664.
- 21 Z. Tian, W. Deng, X. Wang, C. Liu, C. Li, J. Chen, M. Xue, R. Li and F. Pan, *Funct. Mater. Lett.*, 2017, **10**, 1750081.
- 22 L. Zhang, X. Wang, W. Deng, X. Zang, C. Liu, C. Li, J. Chen, M. Xue, R. Li and F. Pan, *Nanoscale*, 2018, **10**, 958–963.
- 23 L. Suo, O. Borodin, W. Sun, X. Fan, C. Yang, F. Wang, T. Gao, Z. Ma, M. A. Schroeder and A. V. Cresce, *Angew. Chem., Int. Ed.*, 2016, **55**, 7136–7141.
- 24 C. Yang, J. Chen, T. Qing, X. Fan, W. Sun, A. von Cresce, M. S. Ding, O. Borodin, J. Vatamanu, M. A. Schroeder, N. Eidson, C. Wang and K. Xu, *Joule*, 2017, **1**, 122–132.
- 25 L. Suo, O. Borodin, T. Gao, M. Olguin, J. Ho, X. Fan, C. Luo, C. Wang and K. Xu, *Science*, 2015, **350**, 938–943.

- 26 L. Suo, O. Borodin, Y. Wang, X. Rong, W. Sun, X. Fan, S. Xu, M. A. Schroeder, A. V. Cresce, F. Wang, C. Yang, Y.-S. Hu, K. Xu and C. Wang, *Adv. Energy Mater.*, 2017, **7**, 1701189.
- 27 Z. Wei, D. Wang, M. Li, Y. Gao, C. Wang, G. Chen and F. Du, *Adv. Energy Mater.*, 2018, **8**, 1801102.
- 28 C. Li, X. Wang, W. Deng, C. Liu, J. Chen, R. Li and M. Xue, *ChemElectroChem*, 2018, **5**, 3887–3892.
- 29 Y. Lu, L. Wang, J. Cheng and J. B. Goodenough, *Chem. Commun.*, 2012, **48**, 6544–6546.
- 30 L. Wang, J. Song, R. Qiao, L. A. Wray, M. A. Hossain, Y.-D. Chuang, W. Yang, Y. Lu, D. Evans and J.-J. Lee, *J. Am. Chem. Soc.*, 2015, **137**, 2548–2554.
- 31 Y. Yamada, K. Usui, K. Sodeyama, S. Ko, Y. Tateyama and A. Yamada, *Nat. Energy*, 2016, **1**, 16129.
- 32 J. Wang, J. Polleux, J. Lim and B. Dunn, *J. Phys. Chem. C*, 2007, **111**, 14925–14931.
- 33 K. Nakamoto, R. Sakamoto, Y. Sawada, M. Ito and S. Okada, *Small Methods*, 2018, **3**, 1800220.
- 34 D. J. Kim, Y. H. Jung, K. K. Bharathi, S. H. Je, D. K. Kim, A. Coskun and J. W. Choi, *Adv. Energy Mater.*, 2014, **4**, 1400133.
- 35 H. Gao and J. B. Goodenough, *Angew. Chem., Int. Ed.*, 2016, **55**, 12768–12772.
- 36 Z. Hou, X. Li, J. Liang, Y. Zhu and Y. Qian, *J. Mater. Chem. A*, 2015, **3**, 1400–1404.
- 37 J. Yue, L. Lin, L. Jiang, Q. Zhang, Y. Tong, L. Suo, Y. s. Hu, H. Li, X. Huang and L. Chen, *Adv. Energy Mater.*, 2020, **10**, 2000665.
- 38 H. Ao, C. Chen, Z. Hou, W. Cai, M. Liu, Y. Jin, X. Zhang, Y. Zhu and Y. Qian, *J. Mater. Chem. A*, 2020, **8**, 14190–14197.
- 39 D. Wang, Q. Liu, C. Chen, M. Li, X. Meng, X. Bie, Y. Wei, Y. Huang, F. Du, C. Wang and G. Chen, *ACS Appl. Mater. Interfaces*, 2016, **8**, 2238–2246.